

Full length article

Design and analysis of a two-dimensional large-scale silicon-photonic optical phased array

Ruitao Jiang^{a,b}, Rui Wang^{a,*}, Jin Guo^a, Haibo Liu^a, Kunyang Du^{a,b}, Yaoyuan Zhang^{a,b}, Yunhan Wu^{a,b}, Yuanyang Li^a

^a State Key Laboratory of Laser Interaction with Matter, Changchun Institute of Optics, Fine Mechanics and Physics, Chinese Academy of Sciences, Changchun 130033, China

^b University of Chinese Academy of Sciences, Beijing 100049, China



ARTICLE INFO

Keywords:

Optical phased array
Silicon photonics devices
Thermo-optic phase shifter
2D beam scanning

ABSTRACT

Currently, two-dimensional (2D) optical phased arrays (OPAs) have broad development prospects in many emerging fields. However, a traditional 2D-OPA sets a phase shifter for each antenna, causing large antenna spacing, high power consumption, and complex wiring. In this study, we first introduce a theoretical model of an $N \times N$ OPA by separating the phase shifter from the antenna element; only 2N phase shifters are used to realize 2D beam scanning, effectively reducing the power consumption and wiring complexity. To reduce the antenna spacing, we next use inverse design and particle swarm optimization to design compact, low-loss, and high-performance silicon-photonic devices, including cross waveguides, Y branches, directional couplers, and grating antennas. For the thermo-optic phase shifter (TOPS), we introduce the semiconductor material AlN that enables the modulation speed to reach 45 kHz. The length of the TOPS is 30 μm and phase-shifting efficiency (P_π) is only 20 mW. Finally, for proof of concept, we built an 8×8 OPA architecture model with an antenna spacing of 8.5 μm . The simulation results show that the OPA achieves $10.5^\circ \times 10.5^\circ$ 2D-beam steering at the 1.55- μm wavelength using only 16 TOPSs, and we use genetic algorithm to realize the sparse uniform array and achieve the side-lobe rejection ratio of 18 dB in the field of view.

1. Introduction

Optical phased arrays (OPAs) [1–26] are optical devices that can realize a beam transceiver and control. These devices have broad development prospects in emerging fields, such as light detection and ranging (LiDAR) system [1–3], three-dimensional (3D) imaging [4], space laser communication [1,2,5], and photonic switching [6,7]. At present, the main types of OPAs include liquid crystal [8], micro-electromechanical systems (MEMS) [9,10], and silicon photonic [2–5,11–22,26]. The response speed of liquid-crystal phased arrays is slow, and the environmental adaptability of MEMS phased arrays needs to be improved, which limits their development in emerging applications. A silicon-photonic phased array can realize chip-level laser scanning; the phase and amplitude of the light radiated from the antenna in this type of array can be independently controlled by the phase shifter, and an electromagnetic wave front of any shape can be formed. Silicon-photonic phased arrays exhibit fast scanning speed, high precision, small size, low cost, and high stability, which meet the needs of beam scanning

technology for emerging applications. Additionally, the manufacture of silicon-photonic phased arrays is fully compatible with complementary metal-oxide semiconductor (CMOS) devices.

Currently, to achieve high beam resolution and a wide two-dimensional (2D) beam scanning range, a variety of OPAs have been reported [2,3,11,13–19,21,22,26]. Although a high-precision and large-angle scanning range is realized by the phase shifter in the vertical antenna direction by using the combination of a one-dimensional (1D) OPA and a tunable laser [2,3,13,18,19,21], the scanning range in the direction parallel to the antenna is limited due to the small tuning range of the laser wavelength. However, to realize high-precision and large-range 2D beam scanning in OPA, it is necessary to have a large-scale integrated antenna array in which the antenna spacing is equal to the wavelength of light. A traditional 2D-OPA [11,14,16,17] realizes 2D beam scanning by setting a phase shifter in each antenna element to independently control the phase and amplitude of the beam. In other words, an $N \times N$ OPA contains N^2 phase shifters, which leads to high power consumption and antenna element spacing. Therefore, a large-

* Corresponding author.

E-mail address: darui9999@163.com (R. Wang).

<https://doi.org/10.1016/j.optlastec.2022.108551>

Received 8 May 2022; Received in revised form 22 July 2022; Accepted 29 July 2022

Available online 12 August 2022

0030-3992/© 2022 Elsevier Ltd. All rights reserved.

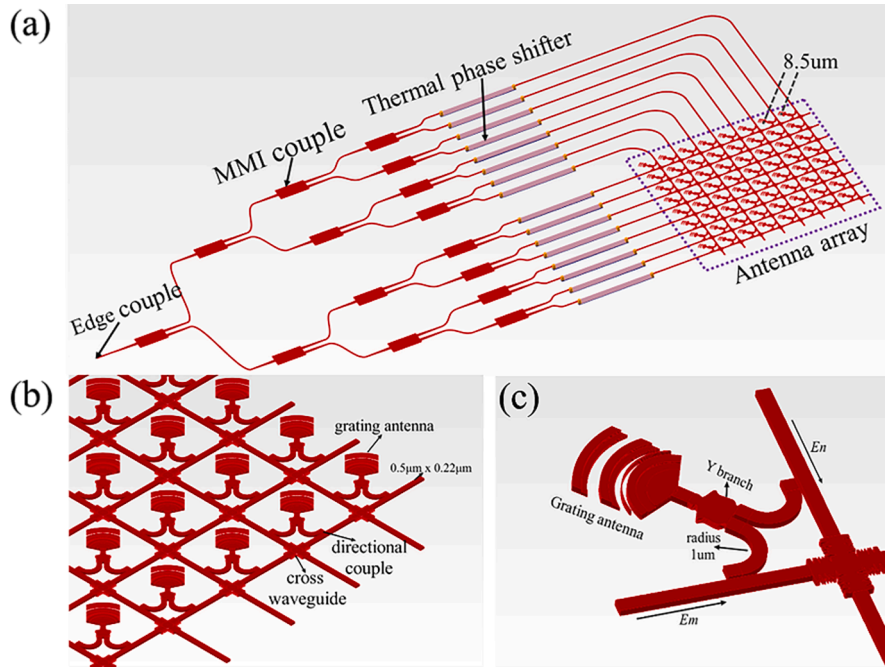


Fig. 1. (a) The proposed 8×8 optical phased array (OPA) structure in which the phase shifter is separated from the antenna element (contains 16 TOPS). (b) Antenna array and (c) antenna element structure diagrams.

scale integrated 2D-OPA with small antenna spacing has not yet been realized.

In this study, we first introduce a 2D-OPA designed by separating the phase shifter from the antenna element. Through theoretical analysis of an $N \times N$ OPA, it is determined that only $2N$ phase shifters can achieve 2D beam scanning. Compared with a traditional 2D-OPA, the power consumption and wiring complexity of the chip are effectively reduced. Using finite-difference time-domain (FDTD) simulations, we discuss the design and simulation of the photonic devices that constitute the OPA, including edge couplers, multimode interference (MMI) couplers, thermo-optic phase shifters (TOPSs), directional couplers (DCs), cross waveguide (CW), Y branch, and grating antenna. The device sizes of the TOPS, DC, Y branch, and CW are reduced as compared to existing devices. Resultant performance parameters include the following: the TOPS modulation speed reaches 45 kHz, the length is $30 \mu\text{m}$, and the loss is 0.04 dB/cm; the coupling length for 100% coupling efficiency of the DC is $3 \mu\text{m}$; the transmittance of the Y branch is 95.1%, and the area is $2.5 \times 1.5 \mu\text{m}^2$; the transmittance of the CW is 95.05%, the reflection is -27 dB , the crosstalk is -33 dB , and the area is $2.5 \times 2.5 \mu\text{m}^2$.

Finally, we established an 8×8 OPA to verify the feasibility of the design scheme. Using the designed photonic device, we obtained an antenna spacing of $8.5 \mu\text{m}$ and a radiation aperture of $68 \mu\text{m} \times 68 \mu\text{m}$. The FDTD simulation results show that the proposed OPA can achieve a 2D beam scanning range of $10.5^\circ \times 10.5^\circ$ with only a single-wavelength light source and 16 TOPSs. The beam full width at half maximum (FWHM) is 1.21° and the side-lobe rejection ratio (SLSR) is 12 dB when the phase difference is zero. At the same time, we use genetic algorithm [38] to realize the sparse uniform array and achieve the SLSR of 18 dB in the field of view. Our results provide a solution for realizing large-scale integrated 2D-OPAs with small antenna spacing.

2. Theoretical analysis and OPA architecture design

Our proposed 2D-OPA architecture is illustrated in Fig. 1(a). The phase shifter is separated from the antenna array element, the OPA couples the off-chip light source into the chip through the edge coupler, and the phase and amplitude of each light beam are tuned by the TOPS and then transmitted to the antenna array. The structures of the

designed antenna array and element are shown in Fig. 1(b) and (c), respectively. As the OPA's 2D beam scanning needs to control the relative phase between adjacent radiation elements, the bus waveguides are cross-arranged; each antenna element is provided with two DCs to couple the optical element of the row and column, which then combines the coupled light through the Y branch and transmits it to the grating antenna. We expand the antenna element shown in Fig. 1(b) to $N \times N$ dimension, assuming that the electric fields of the two transmission light beams coupled by the antenna elements in the M^{th} row and the N^{th} column are written as $E_m = A \exp(i(\phi_m - \omega t))$ and $E_n = A \exp(i(\theta_n - \omega t))$, respectively, where A denotes the amplitude, ϕ_1 and ϕ_2 represent the phases of the transmitted light, and ω indicates the angular frequency. Therefore, the output photoelectric field after the Y branch can be expressed as follows:

$$\begin{aligned} E_{(m,n)} &= \frac{1}{\sqrt{2}}(E_m + E_n) = \frac{1}{\sqrt{2}} \cdot A (\exp(i(\phi_m - \omega t)) + \exp(i(\theta_n - \omega t))) \\ &= \frac{A}{\sqrt{2}} \exp(-i\omega t) \cdot (\exp(i\phi_m) + \exp(i\theta_n)) \\ &= \frac{A}{\sqrt{2}} \exp(-i\omega t) \cdot \cos\left(\frac{\phi_m - \theta_n}{2}\right) \cdot \exp\left(i\left(\frac{\phi_m + \theta_n}{2}\right)\right) \end{aligned} \quad (2.1)$$

The phase of the light radiated by the grating antenna can then be expressed as follows:

$$\psi_{(m,n)} = \arctan\left(\frac{\sin\phi_m + \sin\theta_n}{\cos\phi_m + \cos\theta_n}\right) \quad (2.2)$$

The phase of the optical signal of the bus waveguide is modulated through the TO phase shifter and the beam phase difference between the antenna element and the adjacent element can be expressed as follows:

$$\psi_{(m+1,n)} - \psi_{(m,n)} = \arctan\left(\frac{\sin\phi_{m+1} + \sin\theta_n}{\cos\phi_{m+1} + \cos\theta_n}\right) - \arctan\left(\frac{\sin\phi_m + \sin\theta_n}{\cos\phi_m + \cos\theta_n}\right) \quad (2.3)$$

and

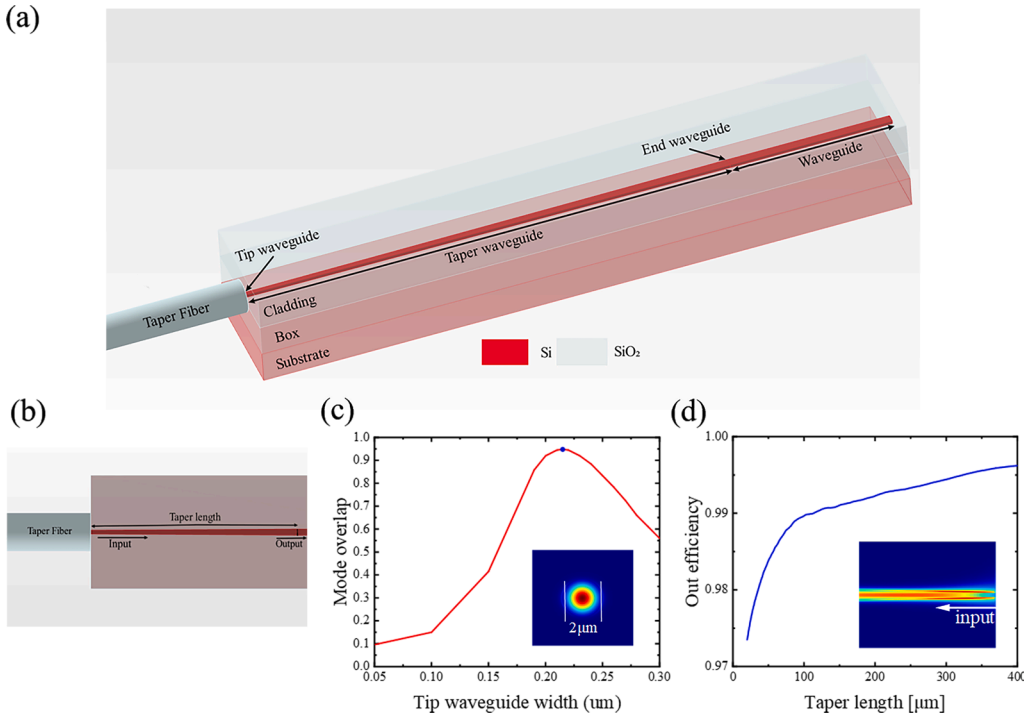


Fig. 2. (a) 3D structure and (b) top view diagrams of the edge coupler. (c) Pattern matching degree between tapered waveguide and tapered fiber with different widths. The pattern distribution at the conical end of the tapered fiber is illustrated. (d) When the input width of the tapered waveguide is 0.21 μm , the coupling efficiency of the edge coupler changes with the length of the waveguide. The illustration shows the electric field simulation diagram of the 300- μm tapered waveguide.

$$\psi_{(m,n+1)} - \psi_{(m,n)} = \arctan\left(\frac{\sin\phi_m + \sin\theta_{n+1}}{\cos\phi_m + \cos\theta_{n+1}}\right) - \arctan\left(\frac{\sin\phi_m + \sin\theta_n}{\cos\phi_m + \cos\theta_n}\right) \quad (2.4)$$

When we make the beam phase difference ($\Delta\phi, \Delta\theta$) constant between the rows and columns of the antenna array in the OPA, from Eqs. (2.3) and (2.4) the phase difference between adjacent antenna elements can be expressed as follows:

$$\Delta\psi_{(1,n)} = \left(1 - \exp\left(\frac{-\Delta\phi}{2}\right)\right) \cdot \exp\left(\frac{\phi_0 + \theta_0}{2}\right) \quad (2.5)$$

and

$$\Delta\psi_{(m,1)} = \left(1 - \exp\left(\frac{-\Delta\theta}{2}\right)\right) \cdot \exp\left(\frac{\phi_0 + \theta_0}{2}\right) \quad (2.6)$$

According to the OPA architecture parameters, the antenna spacing is d , the wavelength of the light source is λ , the phase difference between adjacent antennas is $\Delta\phi, \Delta\theta$, and the deflection angle φ satisfies the following formula:

$$\sin\varphi = \frac{\lambda\Delta\phi}{2\pi d} \quad (2.7)$$

Therefore, when we use the phase shifter to provide an arbitrary phase value in the range of $\sim 0-2\pi$ to the beam, the OPA 2D beam scanning can be realized through 2N phase shifters. Compared with the traditional 2D-OPA, the design scheme effectively reduces power consumption and wiring complexity, but it cannot control the phase of a single antenna element. As obtained from Eq. (2.1), the strength of the main lobe is regulated by phase shifters. To achieve uniform OPA radiation, we gradually increase the coupling length of the DC in the beam

propagation direction to ensure that each antenna element obtains the same optical power. It can be seen from the structure of the antenna array element that the antenna spacing is determined by the CW, DC, Y branch, and grating antenna. Therefore, we applied inverse design and particle swarm optimization (PSO) to achieve compact, high-performance photonic devices, effectively reducing the antenna spacing. Finally, we built an 8×8 OPA architecture based on a 220-nm silicon-on-insulator (SOI) (shown in Fig. 1(a)) containing 16 TOPSs with an antenna spacing of 8.5 μm .

3. Design and simulation of the Silicon-Photonic devices

3.1. Edge coupler

The edge coupler can couple the off-chip light source to the OPA through mode conversion. To improve the coupling efficiency, we designed the optical fiber and input waveguide into tapered structures to match the modes. Fig. 2(a) and (b) shows a schematic diagram of the off-chip coupling structure. The tapered fiber is opposite to the center of the waveguide and the output diameter of the tapered fiber is 2 μm . At the tapered end of the fiber, the fiber cladding and air form the fiber structure, which confines the mode field in the fiber cladding. The diameter of the fiber mode field output is 2 μm , as shown in the inset in Fig. 2(c). To match the modes, the waveguide width was scanned and it was determined that the mode matching degree reached the maximum value of 95% when the width of the tapered waveguide was 0.21 μm . When the input width of the tapered waveguide is 0.21 μm and the output waveguide width is 0.5 μm , the coupling efficiency of the edge coupler varies with the length of the waveguide, as shown in Fig. 2(d).

Table 1

Recent SOI thermo-optical phase shifter and electro-optical phase shifters.

	Phase Shift Materials and Methods	Cladding	Length [μm]	P_x [mW]	τ [μs]	Loss [dB]	V_π [V]
[30]	Ti/TO	Oxide	600	10.6	35	–	4.9
[31]	TiN/TO	Air	1000	0.5	144	0.3	0.9
[32]	N-Si/TO	Air	9.4	12.7	27	0.5	12
[33]	Si/EO	Oxide	1000	1.7	24	3	1.1 _(2x)

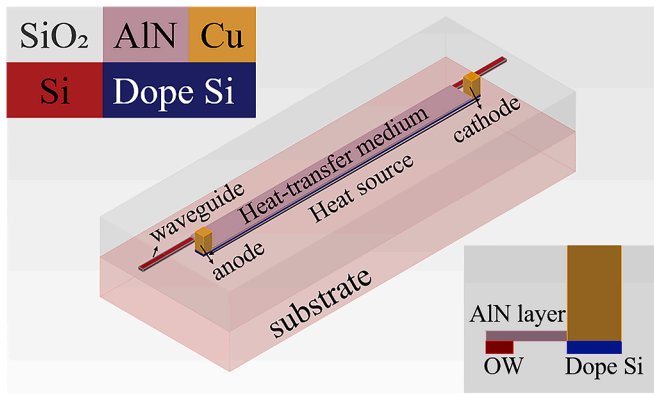


Fig. 3. Structural diagram of the thermo-optic phase shifter.

When the length exceeds 200 μm , the coupling efficiency is greater than 99%. After performing trade-off analysis between on-chip space and coupling efficiency, we chose the length of the tapered waveguide to be 300 μm (coupling efficiency is 99.5% and insertion loss [IL] is 0.02 dB).

3.2. Thermo-Optical phase shifter

The optical phase shifter is an important component of an OPA as it can actively tune the phase of each transmission light beam such that the phased array periodically scans the far-field target. Currently, OPA phase shifters mainly include TOPSs [27-32] and electro-optical phase shifters (EOPSs) [33]. Table 1 summarizes the parameters of phase shifters developed in recent years. The tuning speed of TOPS using metal materials was found to be relatively slow and the overall length reaches several hundreds to thousands of microns. The main reason for this is

that SiO_2 has a very low thermal conductivity of 1.3 W/(m·K). Generally, an EOPS has a fast response speed, a ridge waveguide structure with gradient doping on both sides, and its length is tens of microns. The advantage of an EOPS is that it can reduce the absorption loss of carriers to light, but it is limited by carrier lifetime, which results in a gradual decrease in tuning rate. Moreover, at the junction of a straight waveguide and a ridge waveguide, reflection loss will occur due to the sudden change of the effective refractive index.

After analyzing the advantages and disadvantages of TOPSs and EOPSs, we decided to use doped silicon (DS) as the heat source and aluminum nitride (AlN) to conduct heat and reduce the shortcomings of traditional TOPS, such as slow tuning speed and high π phase shift voltage. The structure of the TOPS is shown in Fig. 3. The DS was placed on the right side of the optical waveguide (OW). For convenience of fabrication, the height of the DS matches that of the OW (0.22 μm). The AlN thermal conductive layer covers the OWs and DS. Because the thermal conductivity of AlN is 285 W/(m·K), which is much larger than that of SiO_2 , it can effectively improve the heat transfer rate and tuning rate. Moreover, it is fully transparent to 1.55- μm infrared light, and the TE fundamental mode effective refractive index of OW using AlN is similar to that using SiO_2 ; it has a low thermo-optical coefficient. Therefore, the optical loss caused by a sudden change of refractive index can be ignored. Most importantly, AlN is also compatible with the CMOS process.

To achieve the optimal structural parameters for the TOPS and corresponding parameters, such as thermal diffusion distribution, modulation efficiency, and response time, the thermal and optical properties of the TOPS were simulated using FDTD. The substrate temperature was set to 300 K, SiO_2 and the air convection was set to 10 W/m²·K, and the OW dimensions were 0.5 μm \times 0.22 μm . N-type DS was used to obtain good electrical conductivity; the selected doping concentration was

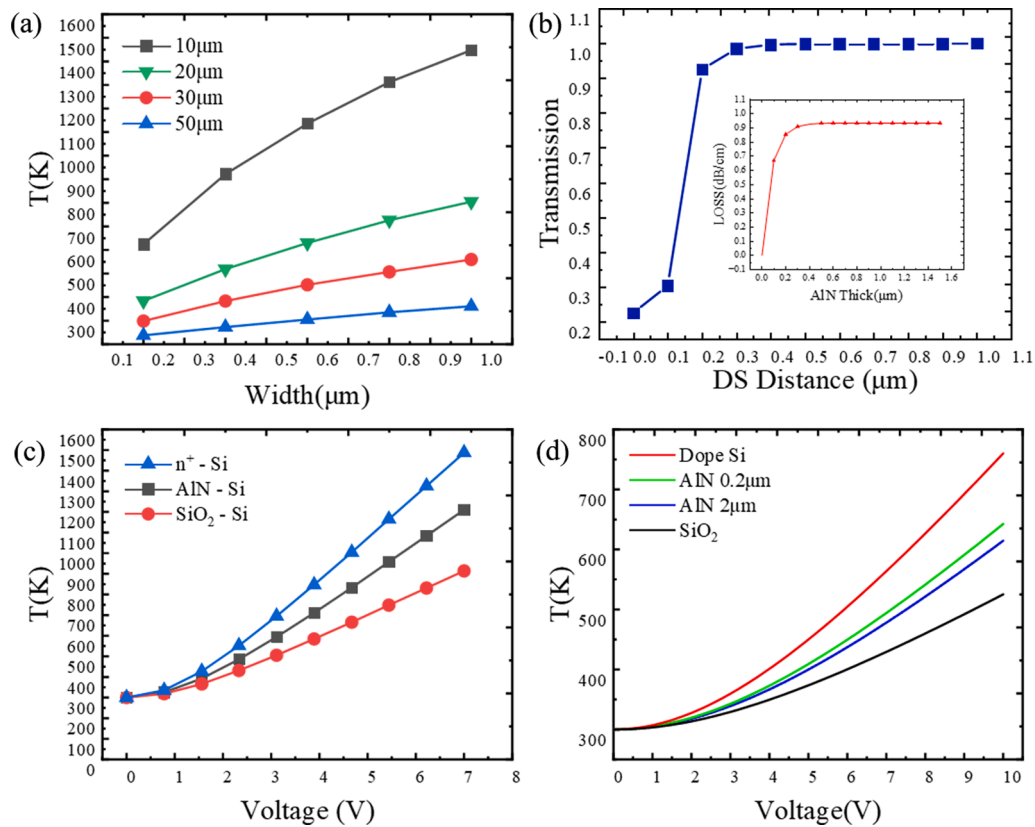


Fig. 4. (a) DS temperature variation with length and width at the same voltage. (b) Transmittance of phase shifter at different spacing doped silicon, and insertion loss of AlN with different thickness. (c) Temperature change of 10- μm DS and of an OW in AlN and SiO_2 thermal conductive media. (d) Temperature variation of 30- μm DS and of an OW in AlN with different thickness.

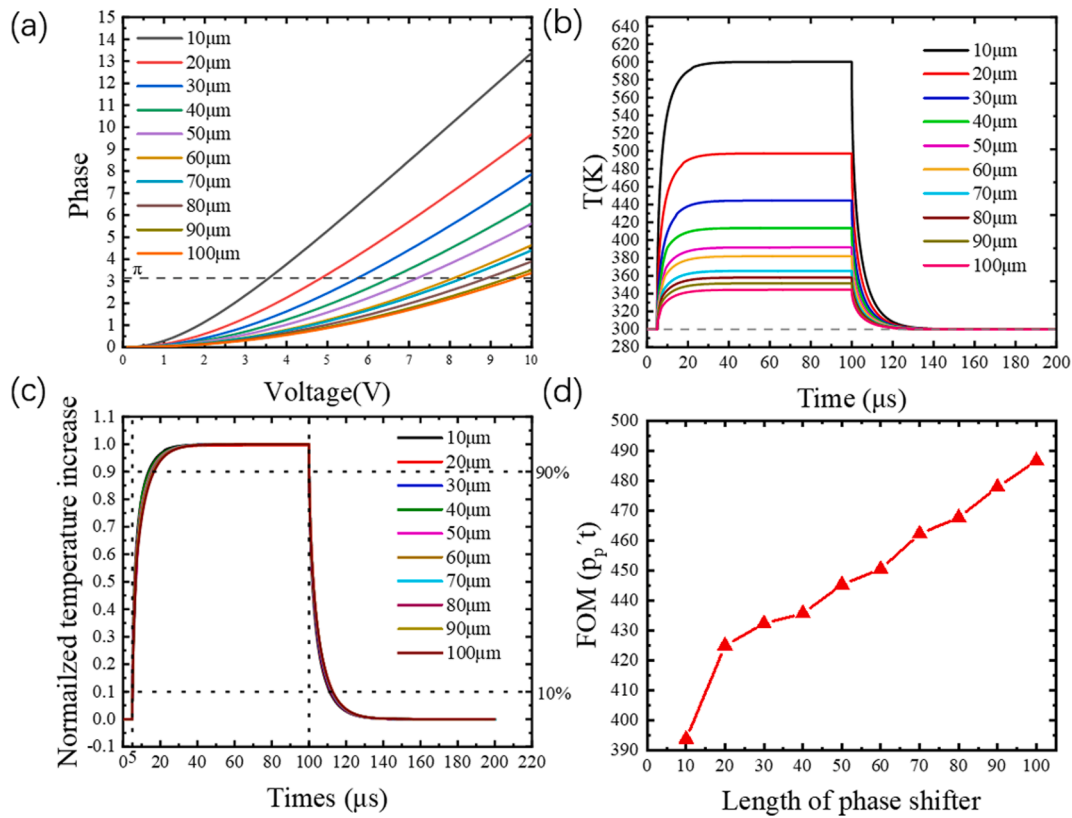


Fig. 5. (a) Phase shifters with varying thickness versus voltage variation. (b) Temperature variation of the π phase shift. (c) Thermal diffusion time (10%–90%) of the π phase shift and (d) FOM values for 10–100 μm TOPSS.

highest at $1e^{20}/(\text{cm}^3)$. Fig. 4(a) shows that under the same voltage, the temperature of DS is inversely proportional to its own resistance. From the research results of Jacques in 2019 [27], the absorption of light by carriers can be avoided when the distance between DS is more than 0.8 μm from the OW. To avoid evanescent wave coupling between the DS and OW, the transmittance of the OW by FDTD simulation is denoted by the blue line in Fig. 4(b). It can be seen that the coupling loss can be ignored when the DS is placed above 0.9 μm on the right side of the OW. Therefore, we set the distance between the DS and the OW to 1 μm to completely eliminate coupling and carrier absorption losses.

The refractive index of AlN is approximately 2.0, and it is fully transparent to light with a wavelength of 1.55 μm . As shown in the illustration in Fig. 4(b), for 1.55- μm transverse electric (TE) mode light, the loss maximum value is 0.93 dB/cm. Therefore, the optical loss caused by the AlN is negligible. Fig. 4(c) shows a schematic diagram of the temperature change of the OW under the two heat-conducting media: AlN and SiO₂. As AlN has extremely high thermal conductivity,

the OW temperature increases from a peak value of 900 K to a peak value of 1200 K when the voltage is at the maximum value. Therefore, the temperature of the OW using AlN heat conduction is closer to the temperature of the DS, which effectively improves heat transfer efficiency. When the length of the DS is 30 μm , the temperature of the OW decreases with the increase in AlN thickness at the same voltage. This occurs because the specific heat capacity of AlN is 748 J/kg·K. However, when the thickness of the AlN thermal conductive medium is the same as the chip cladding, the OW temperature is still much higher than that of SiO₂ used for thermal conduction, as shown in Fig. 4(d). In summary, we considered the chip layout, processing technology, transmission efficiency, and other factors, and chose a DS width of 1 μm , a distance from the OW of 1 μm , and an AlN thickness of 0.2 μm .

Because the heat capacity and resistance of the TOPS increases with length, it requires more heat to reach the temperature at which the π phase shift is achieved. As shown in Fig. 5(a), the π phase shift voltage (V_π) is proportional to the length of the DS, and V_π is 3.55, 4.84, 5.74,

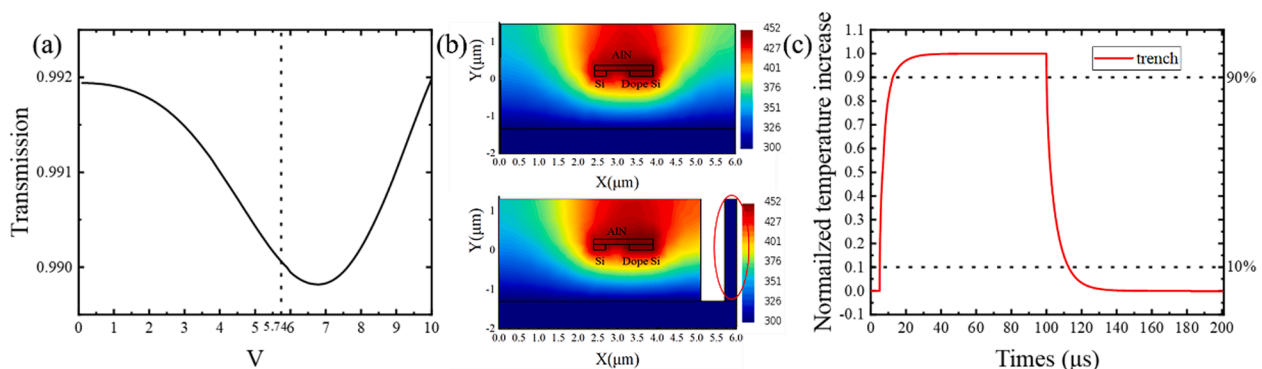


Fig. 6. (a) TOPS light transmittance at different temperatures. (b) Heat distribution diagram of TOPS with or without air grooves. (c) τ of TOPS with air grooves.

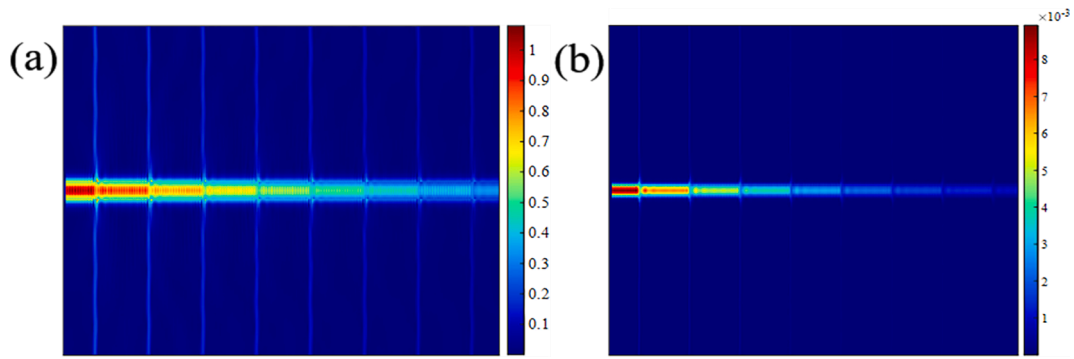


Fig. 7. (a) Electric field and (b) diagram of 1.55- μm mode light.

6.56, 7.21, 8.058, 8.30, 8.90, 9.40, and 9.63 V. Fig. 5(b) and (c) shows the changes in π phase shift temperature and thermal diffusion time (τ) for TOPSs with different lengths using the AlN heat-conducting medium. τ is proportional to the length of the TOPS and for 10%–90% of the OW temperature response, the sum of the rise and fall times ($\tau = \tau_r + \tau_f$) is 19.68, 21.24, 21.61, 21.78, 22.26, 22.52, 23.11, 23.38, 23.89, and 24.33 μs . The modulation speed of the TOPS can reach 50 kHz (10 μm) to 40 kHz (100 μm). The efficiency and speed of the TOPS are determined by the figure of merit (FOM) [27] ($FOM = P_\pi \times \tau$); a smaller FOM value represents better TOPS performance. As $P_\pi = G \cdot \Delta T_\pi \cdot A$, where G is the thermal conductivity, T is the temperature change of the π phase shift, and A is the area through which the heat flow passes, the DS length does not affect the power consumption of the TOPS. In Fig. 5(d), the average power of the π phase shift for TOPSs with different lengths is 20 mW. Therefore, the main factor that affects the FOM value is the thermal diffusion time of the TOPS.

Based on the above data, we conducted a trade-off analysis between the size and performance of the TOPS. It was determined that the overall size of the TOPS should be 30 $\mu\text{m} \times 2 \mu\text{m} \times 0.42 \mu\text{m}$, of which the DS and AlN sizes are 30 $\mu\text{m} \times 1 \mu\text{m} \times 0.22 \mu\text{m}$ and 30 $\mu\text{m} \times 2 \mu\text{m} \times 0.2 \mu\text{m}$, respectively. The P_π of the TOPS is 20 mW, the V_π is 5.74 V, and the τ is 21.61 μs . Under these conditions, a modulation speed of 42 kHz can be

achieved. Compared with SiO₂ thermal conductive medium, V_π and P_π are reduced by 5 V and 15 mW, respectively, and the temperature peak of the π phase shift is 445 K, which will not burn out the OPA device. In Fig. 6(a), the transmittance of the TOPS simulated by 3D-FDTD for 1.55- μm TE mode light is between 99% and 99.2%, and the average IL is 0.04 dB/cm.

When the TOPS are densely arranged, air grooves are added around the TOPS to reduce the thermal crosstalk problem because air has an extremely low thermal conductivity of 0.0263 W/(m·k). The groove size is 40 $\mu\text{m} \times 1 \mu\text{m} \times 2 \mu\text{m}$. Fig. 6(b) shows a schematic diagram of the TOPS heat distribution with or without air grooves. The temperature at the position of the red circle in the figure is 301 K and the OW temperature is 452 K, which is 7 K higher than that without air grooves. Therefore, the air groove effectively isolates thermal crosstalk between the TOPSs. The thermal diffusion time is shown in Fig. 6(c), τ_r is 7.52 μs and τ_f is 12.5 μs . Compared with TOPS without air grooves, τ_r decreases by 2.52 μs , τ_f increases by 0.7 μs , τ is 20.02 μs , and the modulation speed is 46 kHz.

3.3. Cross waveguide

From Fig. 1(b), the CW is an important factor restricting the large-

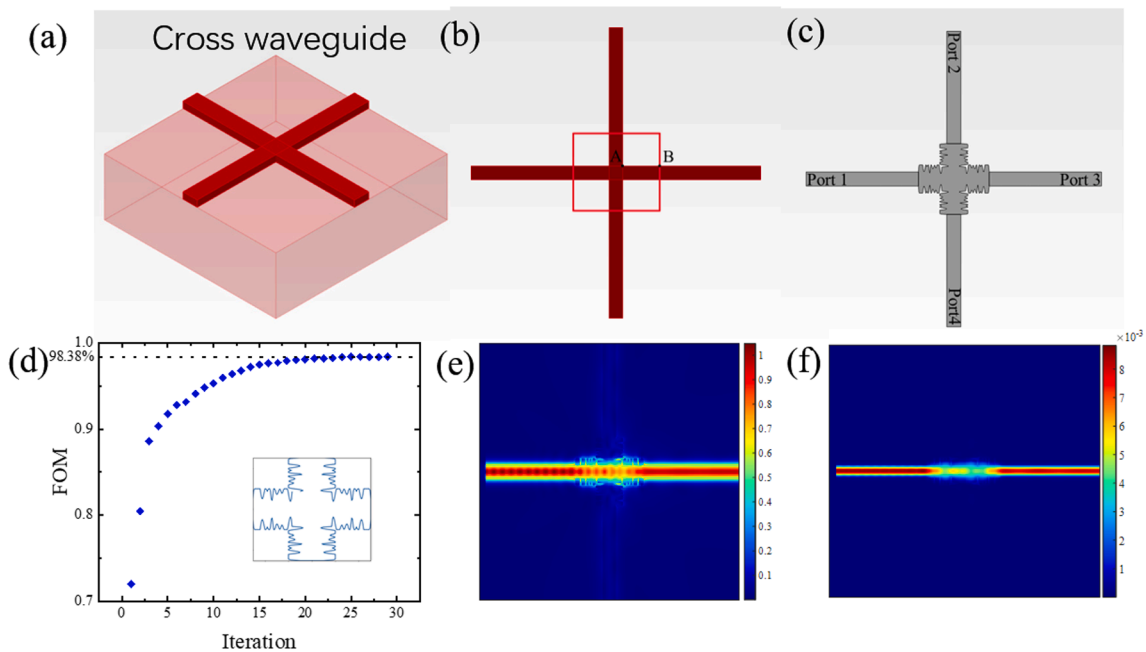


Fig. 8. (a) 3D structure and (b) top view of the vertical intersection of the waveguides. (c) Top view of the optimized crossed waveguide. (d) The FOM value varies with the number of iterations; inset shows the crossed structure corresponding to the optimal value. (e, f) Electric field and power diagrams of the 1.55- μm mode light.

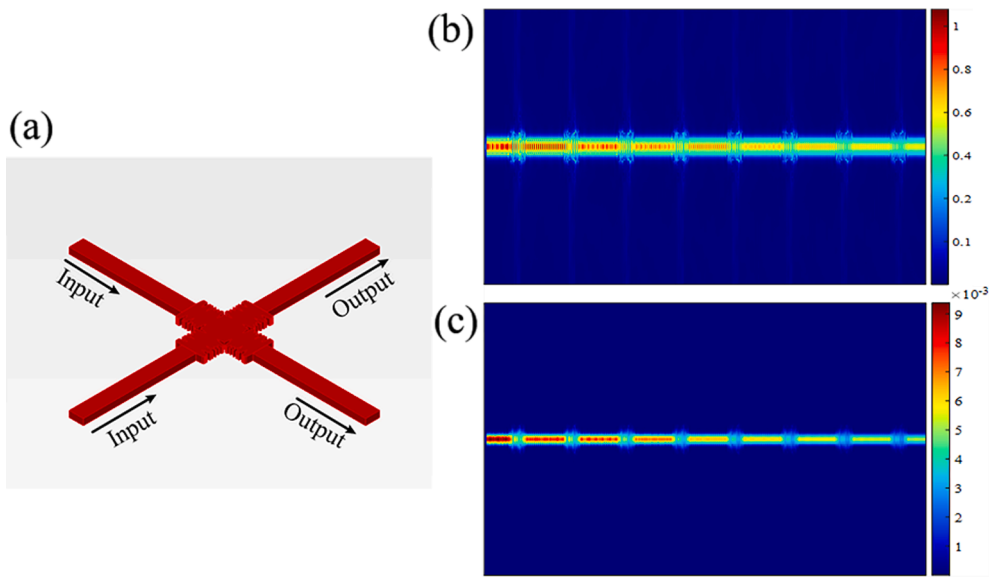


Fig. 9. (a) 3D structural diagram of the CW. (b, c) Electric field and power diagrams of 1.55- μm mode light.

scale expansion of the OPA. In the high-contrast SOI structure, a vertical cross of strip waveguides will destroy the transverse restriction of the waveguide to the transmitted light, resulting in diffraction loss and transverse scattering loss. For the size of waveguide is $0.5\ \mu\text{m} \times 0.22\ \mu\text{m}$, the IL and crosstalk loss (CL) obtained by FDTD simulation are 1.4 dB (72%) and -9 dB. Fig. 7 shows the electric field and power diagram obtained by 1.55- μm TE mode light when eight direct waveguide intersecting structures are linked together. The diffraction and transverse scattering loss of light can be clearly seen; therefore, it is necessary to design and optimize the CW.

Here, we used the reverse design method to design the CW[34,35]

and the objective function was optimized by FDTD and parameter optimization. Fig. 8(a) is a 3D illustration of the CW; the height is $0.22\ \mu\text{m}$ and the design area of the device is $2.5\ \mu\text{m} \times 2.5\ \mu\text{m}$. Because the CW is both axisymmetric and centrosymmetric, we only need to optimize one-eighth of the CW. In the initial optimization parameters and boundary value settings for the AB section of the waveguide, the curve AB is defined by 10 points, the abscissa interval of the curve is $[0.25\ \mu\text{m}, 1.25\ \mu\text{m}]$, the ordinate interval is $[0.25\ \mu\text{m}, 0.45\ \mu\text{m}]$, and the optimized boundary conditions are $[0.2\ \mu\text{m}, 0.5\ \mu\text{m}]$. The abscissa and corresponding ordinate of 10 coordinate points are optimized by PSO, and the width of the silicon photonic device at each coordinate point can be

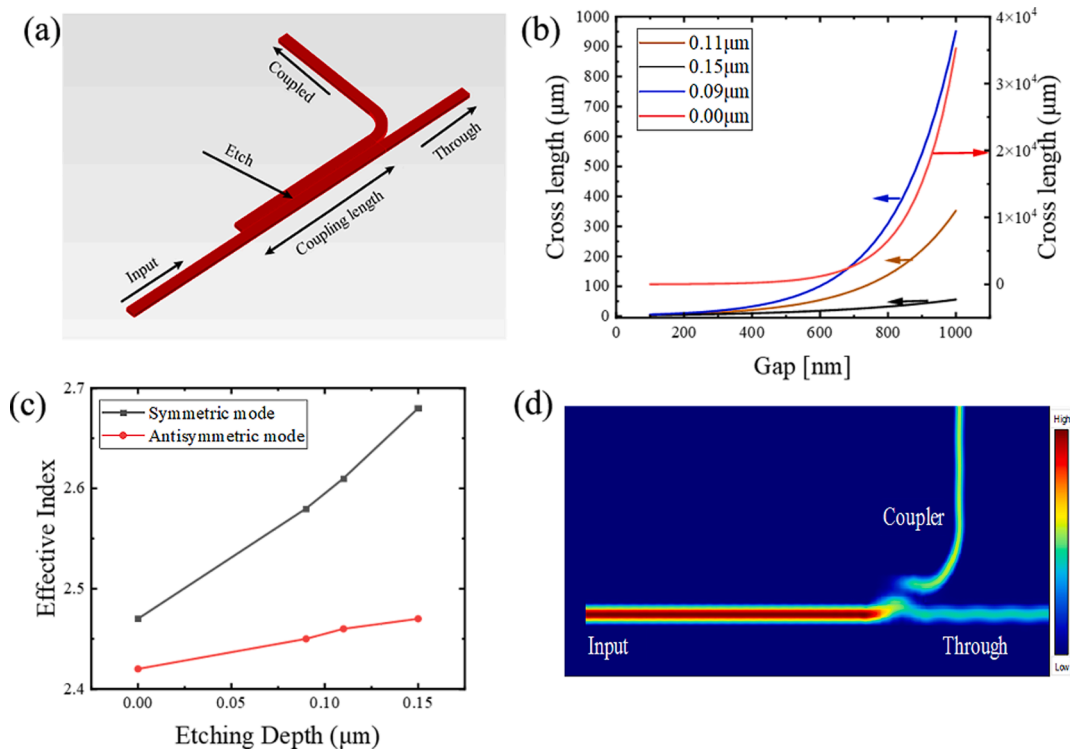


Fig. 10. (a) Schematic diagram of the designed DC structure. (b) Variation of the coupling length for different gaps and etch depths under the parameters $\lambda = 1.55\ \mu\text{m}$, $w = 0.5\ \mu\text{m}$, and $h = 0.22\ \mu\text{m}$ of DC. (c) Effective refractive index of symmetric and antisymmetric modes, with varying etching depth. (d) Electric field transfer diagram at a wavelength of $1.55\ \mu\text{m}$.

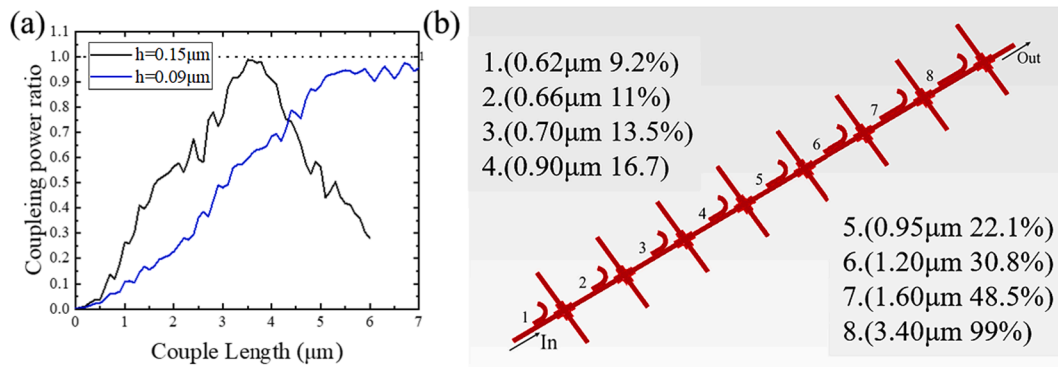


Fig. 11. (a) Coupling efficiencies of DCs with different lengths at etching depths of 0.09 and 0.15 μm. (b) Schematic diagram of the arrangement of coupled structures.

obtained. To obtain a smooth geometric edge curve, we used cubic spline interpolation and take the number of nodes as 50. The FOM value of the CW is defined as the transmittance of port 3, $FOM = T_3(\lambda)$. The simulation results under 2.5D FDTD show that when the wavelength is 1.55 μm, the maximum transmittance of the CW is 98.38%, the IL is 0.07 dB, the reflection is -27 dB, and the CL is -33 dB. The change in the FOM value is shown in Fig. 2(d).

Fig. 9(a) illustrates a 3D structural diagram of the optimized CW. The 3D-FDTD simulation results show that when the wavelength is 1.55 μm, transmittance is 95.05%, reflectivity is 0.2%, IL is 0.22 dB, and CL is -33.1 dB, which is 27% higher than the transmittance of the direct crossing of the waveguide. Fig. 9(b) and (c) shows the electric field diagram and power diagram obtained when eight CWs are linked together. When compared with Fig. 7, it can be seen that the diffraction loss and CL are significantly reduced.

3.4. Directional coupler

There are two DCs in each antenna element, which respectively couple the two transmission lights. The structure is shown in Fig. 10(a);

the width of the coupling waveguide is 0.5 μm. Based on the analysis of coupling theory, the coupling efficiency can be expressed as follows:

$$K^2 = \frac{P_c}{P_0} = \sin^2\left(\frac{\pi \Delta n \cdot L}{\lambda}\right) = \sin^2\left(\frac{\pi L}{2 L_\pi}\right) \quad (3.1)$$

where P_0 is the input optical power, P_c is the optical power coupled into another waveguide, L is the length of the DC, Δn is the difference between the effective refractive indices of the symmetric mode and the antisymmetric mode ($\Delta n = n_1 - n_2$), and L_π is the coupling length. From Eq. (3.1), it is clear that L_π can be reduced by increasing the Δn .

Using FDTD simulations, we found that the use of shallow etching technology in the coupling gap can increase the Δn and reduce the coupling length of the DC. Fig. 10(a) shows the designed DC. Fig. 10(b) and (c) show that as the etching depth decreases, Δn gradually increases. Taking the gap as 0.1 μm, the etching height of the fabrication process is 0.09 μm or 0.15 μm. The L_π of the different etching heights are $L_{\pi_0} = 15.5 \mu\text{m}$, $L_{\pi_{0.11}} = 5.17 \mu\text{m}$, and $L_{\pi_{0.15}} = 3.17 \mu\text{m}$; with the increase of etching height, L_π of the DC is obviously shortened, which is in line with the theoretical analysis. When the length of the coupling region is 10

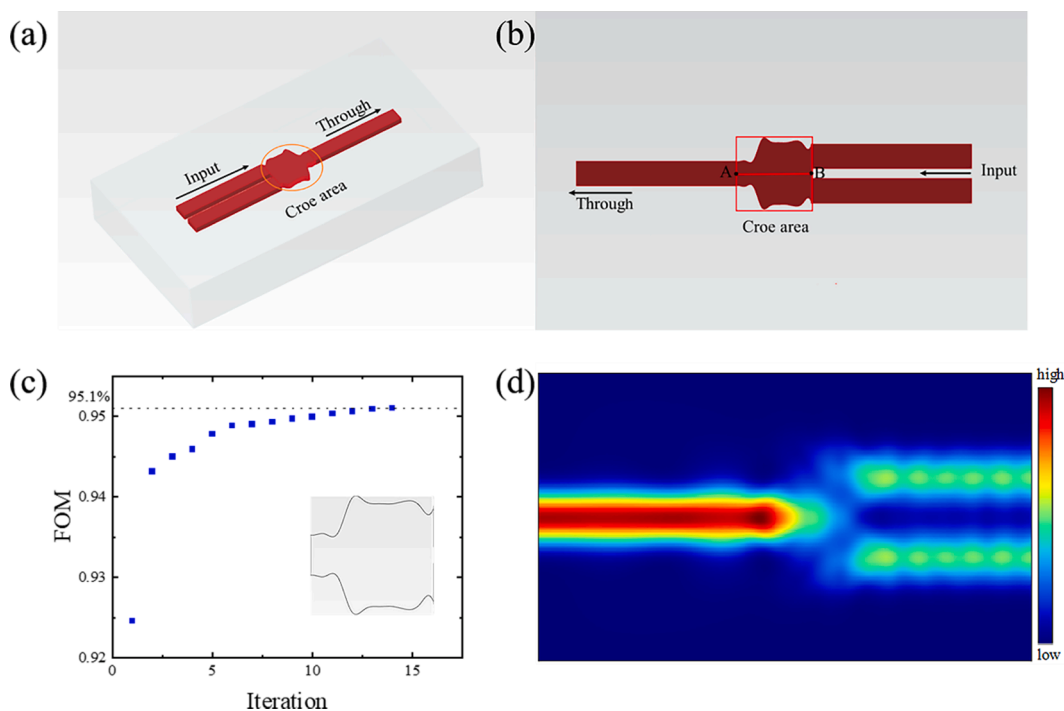


Fig. 12. (a) Schematic diagram of the 3D structure and (b) top view of the optimized Y branch. (c) FOM value as a function of the number of iterations; the inset is a schematic diagram of the optimal Y branch core structure. (d) Electric field transfer diagram of 1.55-μm mode light.

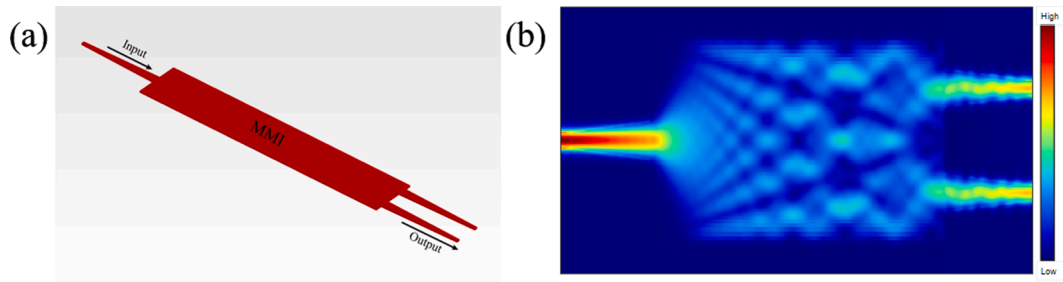


Fig. 13. (a) Schematic diagram and (b) electric field transport of the 1×2 MMI structure.

μm , the IL is $IL_{0.09} = 0.06$ dB and $IL_{0.15} = 0.002$ dB.

In the direction of light transmission, we need to gradually increase the length of the DC so that the radiated power of each antenna element is the same. Fig. 11(a) shows the coupling efficiency of DCs with different etching heights. Although the coupling efficiency curve with an etch height of $0.09 \mu\text{m}$ is smoother, the efficiency curve with an etch height of $0.15 \mu\text{m}$ has a shorter coupling length and lower loss. Therefore, an etching height of $0.15 \mu\text{m}$ was selected. After introducing the CW S-parameters, the distribution of the DC in the transmission direction is shown in Fig. 11(b). The values in the figure represent the DC coupling length and coupling efficiency.

3.5. Y branch

We also used inverse design for the Y branch. Fig. 12(a) and (b) shows a structural schematic diagram and the top view of the designed Y branch. The core area of the device is $1.5 \mu\text{m} \times 1.4 \mu\text{m}$ and the height is $0.22 \mu\text{m}$. In the initial optimization parameters and boundary value settings for the Y branch core area, curve AB is defined by 10 points; the abscissa interval of the curve is $[-0.75 \mu\text{m}, 0.75 \mu\text{m}]$, the ordinate interval is $[0.25 \mu\text{m}, 0.6 \mu\text{m}]$, and the boundary condition is $[0.2 \mu\text{m}, 0.8 \mu\text{m}]$. By optimizing the abscissa and the corresponding ordinate value of each coordinate point by PSO, the width of the Y branch core area at the coordinate point can be obtained, we used cubic spline interpolation and take the number of nodes as 50. The FOM value of the Y branch is defined as the transmittance of the output port, $FOM = T_{\text{through}}$. The change in the FOM value with the number of iterations during the optimization process is shown in Fig. 12(c). The FDTD simulation results show that for the $1.55\text{-}\mu\text{m}$ TE mode light, the maximum transmittance is 95.1%, reflectivity is 0.78%, IL is 0.22 dB, and device area is $2.5 \mu\text{m} \times 1.4 \mu\text{m}$.

3.6. Multimode interference coupler

The MMI coupler is also one of the components in the OPA. A 1×2 MMI coupler with intermediate incidence was used in the present study and the length of the coupling region was calculated to be $36 \mu\text{m}$. Both the input and output ends adopt a tapered structure. The FDTD simulation results show that when the width, length, and spacing of the tapered waveguide are $2.2 \mu\text{m}$, $10 \mu\text{m}$ and $3.1 \mu\text{m}$, respectively, the lowest IL values of 0.02 dB, 0.07 dB, and 0.01 dB, are obtained. Fig. 13 (a) shows a structural diagram of the optimal MMI coupler for the $1.55\text{-}\mu\text{m}$ TE mode light. The area of the MMI coupler is $56 \mu\text{m} \times 6 \mu\text{m}$ and the transmittance is 96.8%.

3.7. Grating coupler optical antenna

Grating couplers are mainly used as antennas in 2D-OPA [11,14,16,17,36]. In our previous work [37], we designed a grating antenna based on a 300-nm SOI. When the number of grating teeth is equal to three, we can obtain 57.2% upward radiation efficiency. The area of the structure is $2.72 \mu\text{m} \times 2.44 \mu\text{m}$ and a schematic of the structure is shown in Fig. 14.



Fig. 14. Grating antennas under 300-nm SOI.

Table 2
Grating coupler optical antenna structure parameters (μm).

R	θ	W_1	W_2	W_3	W_4	h_1	h_2	et_1	et_2
1	140°	0.35	0.3	0.2	0.03	0.15	0.12	0.6	0.16

In this study, we design the grating antenna under 220-nm SOI and optimized it using PSO. The number of particles and iterations is 20 and 50 respectively. The parameters to be optimized are the radius R and central angle θ of the sector surface, the widths W_2 , W_4 and spacing et_1 , et_2 of the grating teeth, and the widths W_1 , W_3 and height h_1 , h_2 of the etched area. To achieve the maximum upward radiation efficiency of the grating antenna for simulation, we did not consider the process standard, and the structural parameters are summarized in Table 2. The grating antenna structure is shown in Fig. 15(a); the number of periods is three, area is $3.45 \mu\text{m} \times 3.1 \mu\text{m}$, upward emissivity (T_{up}) is 59%, downward emissivity (T_{down}) is 20.2%, reflectivity is 0.61%, transmittance is 12.1%, and edge scattering rate is 4.25%. Fig. 15(d) and (e) shows the radiation patterns of the near-field and far-field of a single grating antenna; the diffraction angle is 21° .

Under the grating structure in Fig. 15, we introduce the process standard again, and run PSO again. The optimized grating antenna structure is shown in Fig. 16, and the structure parameters are in Table 3. The number of periods is three, area is $3 \mu\text{m} \times 2.8 \mu\text{m}$, T_{up} is 53.3%, T_{down} is 21.6%, reflectivity is 0.5%, transmittance is 10.1%, and edge scattering rate is 5.2%.

4. Simulation and analysis of the OPA

Based on the OPA architecture shown in Fig. 1(a), we built an 8×8 OPA using the designed photonic device with an antenna spacing of $8.5 \mu\text{m}$ to verify the feasibility of the design scheme via FDTD simulations. To realize 2D scanning at any angle by controlling the phase, we

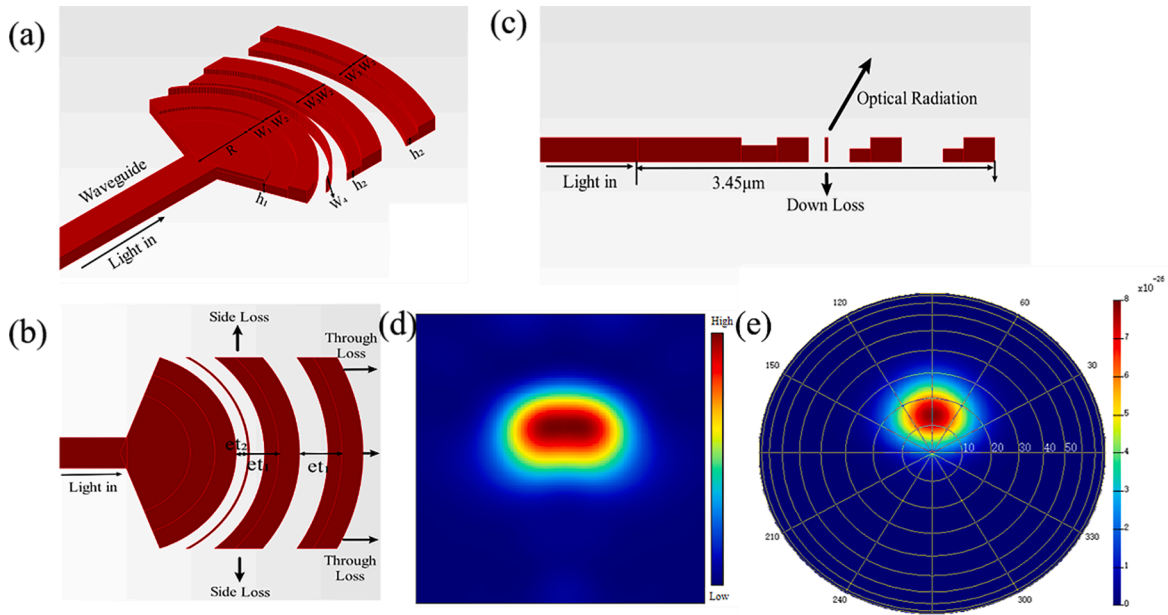


Fig. 15. (a) 3D structural diagram, (b) top view, (c) side view, (d) near-field emission patterns, and (e) far-field radiation patterns of the grating antenna.

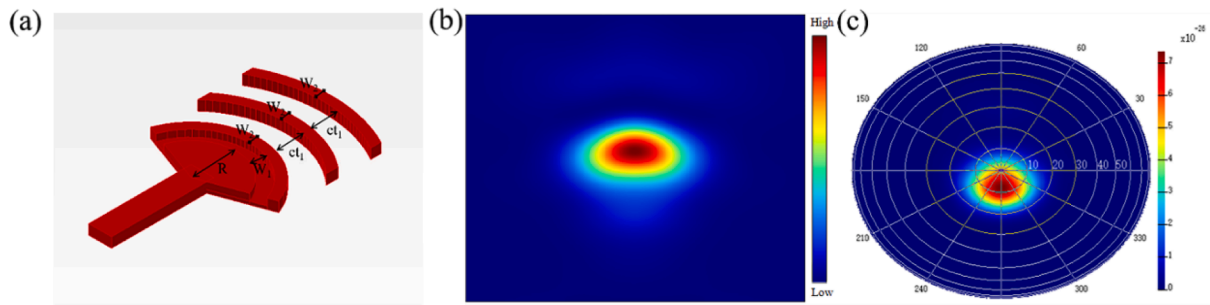


Fig. 16. (a) 3D structural diagram, (b) near-field emission patterns, and (c) far-field radiation patterns of the grating antenna.

Table 3

Grating coupler optical antenna structure parameters (μm).

R	θ	W_1	W_2	W_3	W_4	h_1	h_2	ct_1	ct_2
1	140°	0.3	0.2	0	0	0.11	0	0.6	0

calculated that when the far-field main lobe deflects 4° along the transverse (longitudinal) direction, the lateral or longitudinal phase difference of the beam is $23/30\pi$. The TOPS was controlled to adjust the phase difference between the beams to be $23/30\pi$, and the far-field radiation pattern of the array for data processing to remove the grating lobes was obtained, as shown in Fig. 17. The simulation results are

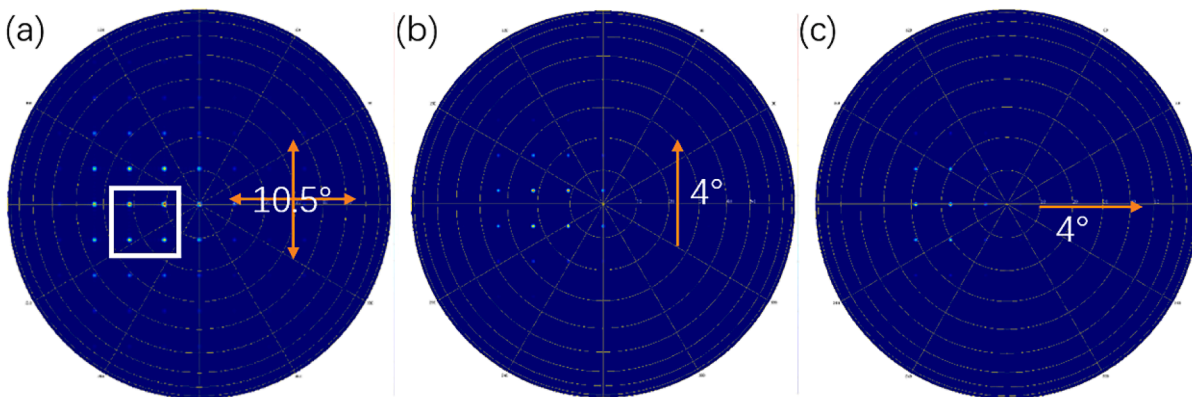


Fig. 17. Far-field main lobe laterally shifted by adjusting the beam phase. (a) Phase difference of zero, (b) lateral phase difference of $23/30\pi$, and (c) longitudinal phase difference of $23/30\pi$.

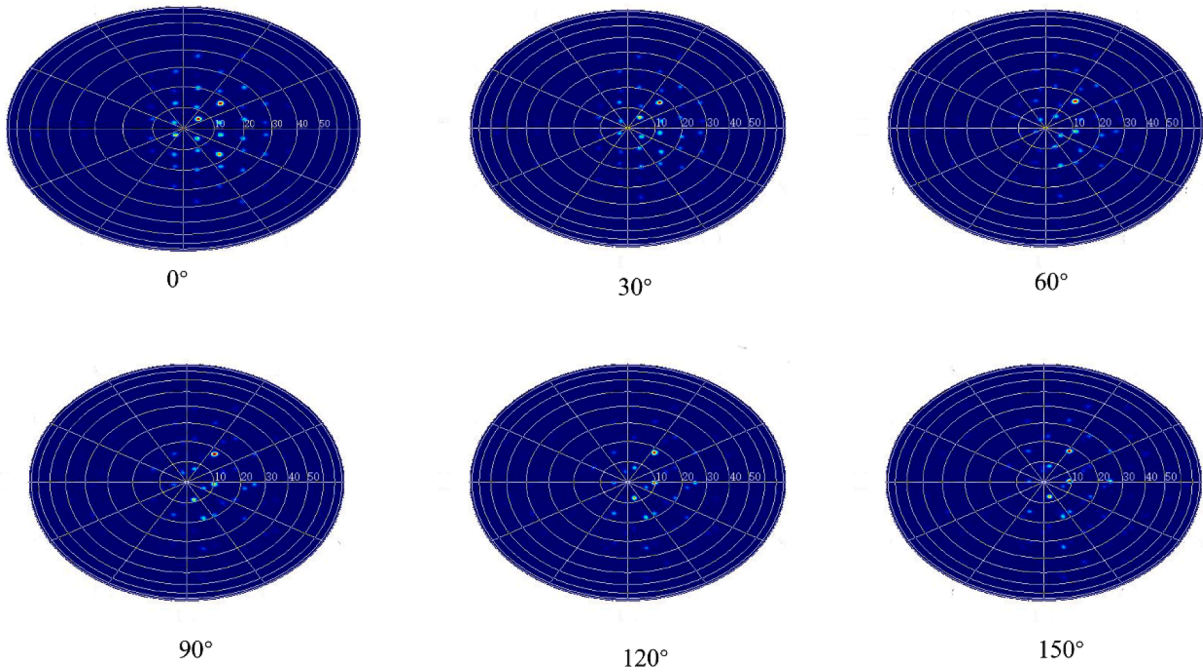


Fig. 18. Far-field profile of the 8×8 OPA obtained by Fourier transform.

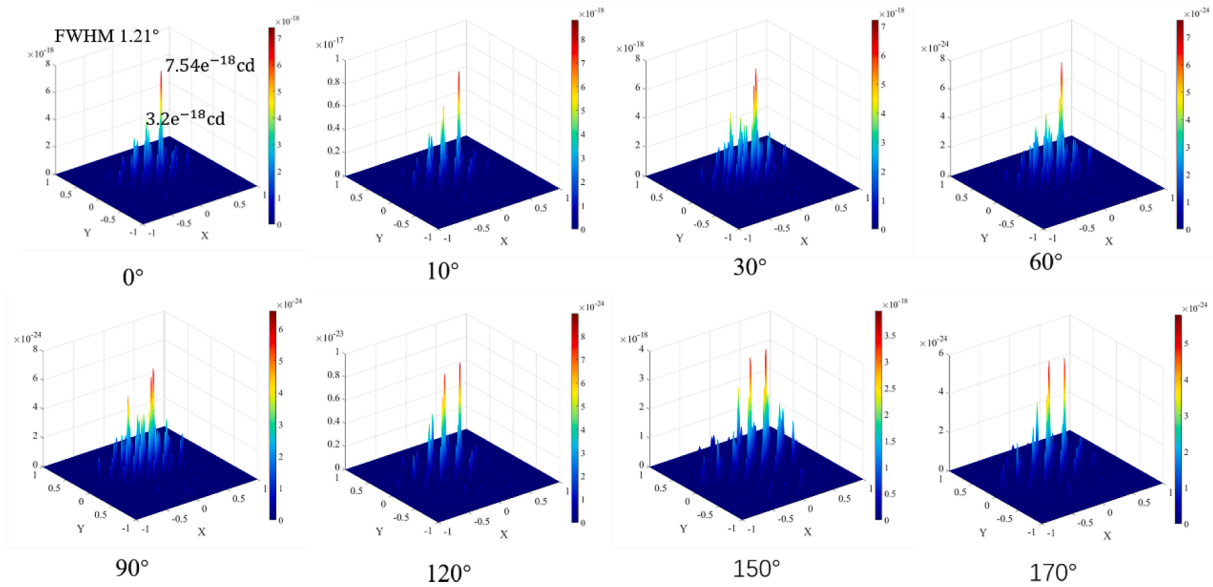


Fig. 19. Far-field 3D radiation patterns of the 8×8 OPA with different phases.

consistent with the theoretical calculations.

We deflect the beam by changing the phase difference of the horizontal and vertical beams using the TOPS. When the beam phase difference is $0^\circ, 10^\circ, 30^\circ, 60^\circ, 90^\circ, 120^\circ, 150^\circ,$ and 170° , it is evident from the far-field profile of the OPA obtained by the Fourier transform (Fig. 18) that the main lobe of the far-field beam moves obliquely upward as the phase changes. Fig. 19 shows the far-field 3D radiation patterns of the OPA with different phases. Because the OPA is non-apodized, near-field emission of uniform energy and the grating lobe energy in the far-field distribution diagram is relatively strong. With movement of the main lobe, the intensity of the first main maxima is gradually the same as that of the main lobe. When the phase difference is 170° , the intensities of the two are approximately the same and the moving angle of the main lobe is approximately $4.9^\circ \times 4.9^\circ$. The

simulation results are consistent with the calculation results of Eq. (2.7). Using the far-field 3D radiation data in Fig. 19, we calculated that when the phase difference is zero, the SLSR value is a maximum of 12 dB and the SLSR gradually decreases as the steer angle increases.

We designed the OPA to be a uniform array and equal power emission, and grating lobes cannot be avoided. Therefore, to achieve the purpose of suppressing the OPA side lobe level in the field of view, we use genetic algorithm to sparsely optimize the array antenna structure. We set $f_{mn} = 1$ to represent to have the grating antenna, and $f_{mn} = 0$ to have no grating antenna, and the far-field pattern function $F(\varphi, \theta)$ of the OPA is:

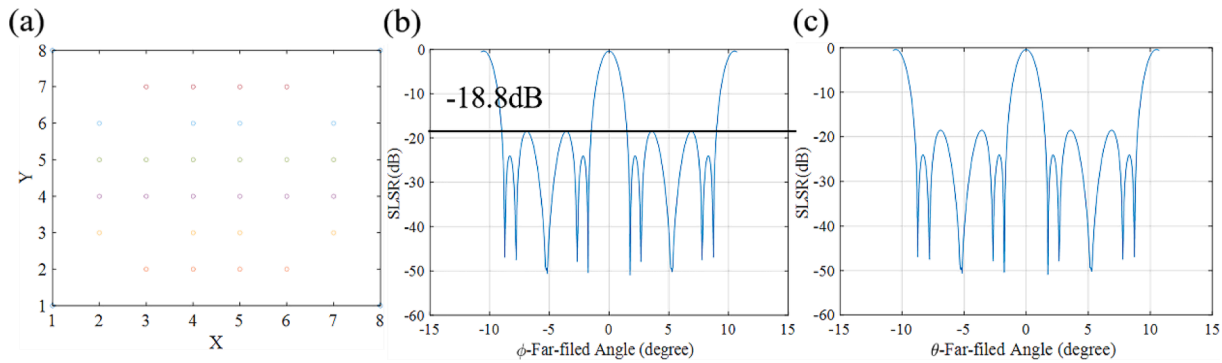


Fig. 20. (a) Schematic diagram of antenna array structure, (b) ϕ -far-field antenna pattern, and (c) θ -far-field radiation patterns.

$$F(\varphi, \theta) = f_{mm} \bullet \sum_{n=0}^{N-1} \sum_{m=0}^{M-1} \exp(j \frac{2\pi}{\lambda} (d_m (\cos\theta \sin\varphi - \cos\theta_0 \sin\varphi_0) + d_n (\sin\theta - \sin\theta_0)))$$

φ is horizontal azimuth, θ is pitch angles, θ_0 and φ_0 is main lobe direction, d_m and d_n is antenna distance. The optimization model is defined as: $\min MSL$, where MSL is the sum of the maximum side lobe level of the pattern and the maximum side lobe level of the elevation pattern. The structure diagram of the optimized antenna array is shown in Fig. 20 (a). Compared with Fig. 19, that the side lobe level is effectively reduced and the SLSR of -18.8 dB is achieved. It can be seen from the far-field pattern in Fig. 20(b) and (c).

5. Conclusion

In this study, we proposed a 2D-OPA architecture scheme that separates the phase shifter from the antenna element and designed a compact and high-performance silicon-photonics device. We placed the TOPS on the bus waveguide to control the phase of the transverse and longitudinal beams. Via theoretical analysis, $N \times N$ OPA 2D scanning was realized using only $2N$ TOPSs. We used the designed silicon-photonics device to integrate an 8×8 OPA architecture with 16 TOPSs. Simulation results show a 2D beam scanning range of $10.5^\circ \times 10.5^\circ$, an FWHM of 1.21° , and a maximum SLSR of 12 dB.

We use the genetic algorithm to obtain the sparse layout of the uniform array, and realize the SLSR of -18.8 dB. In summary, we controlled the phase of the light wave through the TOPS, realized 2D scanning of the OPA, determined the feasibility of the 2D-OPA, and proposed a feasible solution to miniaturize the OPA array element spacing.

Funding

Funding of “Xuguang Talents” from CIOMP; Industrial Innovation Project of Jilin Development and Reform Commission (2202C046-2).

Declaration of Competing Interest

The authors declare that they have no known competing financial interests or personal relationships that could have appeared to influence the work reported in this paper.

Data availability

Data will be made available on request.

References

- [1] Y. Wu, S. Shao, Y. Li, X. Chen, D. Che, J. Chen, K. Du, R. Jiang, X. Huang, D. Kan, Multi-beam optical phase array for long-range LiDAR and free-space data communication, *Opt. Laser Technol.* 151 (2022) 108027, <https://doi.org/10.1016/j.optlastec.2022.108027>.
- [2] C.V. Poulton, M.J. Byrd, P. Russo, E. Timurdogan, M. Khandaker, D. Vermeulen, M. R. Watts, Long-range LiDAR and free-space data communication with high-performance optical phased arrays, *IEEE J. Sel. Top. Quant. Electron.* 25 (5) (2019) 1–8.
- [3] C.V. Poulton, A. Yaacobi, D.B. Cole, M.J. Byrd, M. Raval, D. Vermeulen, M. R. Watts, Coherent solid-state LiDAR with silicon photonic optical phased arrays, *Opt. Lett.* 42 (20) (2017) 4091.
- [4] F. Aflatouni, B. Abiri, A. Rekh, A. Hajimiri, Nanophotonic projection system, *Opt. Exp.* 23 (2015) 21012–21022, <https://doi.org/10.1364/OE.23.021012>.
- [5] W.S. Rabinovich, P.G. Goetz, M. Pruessner, R. Mahon, M.S. Ferraro, D. Park, E. Fleet, M.J. DePrenger, Free space optical communication link using a silicon photonic optical phased array, *Proc. SPIE* (2015), <https://doi.org/10.1117/12.2077222>.
- [6] M.-J. Kwack, T. Tanemura, A. Higo, Y. Nakano, Monolithic InP strictly non-blocking 8×8 switch for high-speed WDM optical interconnection, *Opt. Exp.* 20 (2012) 28734–28741, <https://doi.org/10.1364/OE.20.028734>.
- [7] T. Tanemura, I.M. Soganci, T. Oyama, T. Ohyama, S. Mino, K.A. Williams, N. Calabretta, H.J.S. Dorren, Y. Nakano, Large-capacity compact optical buffer based on InP integrated phased-array switch and coiled fiber delay lines, *J. Lightwave Technol.* 29 (2011) 396–402, <https://doi.org/10.1109/JLT.2010.2102338>.
- [8] R.A. Meyer, Optical beam steering using a multichannel lithium tantalate crystal, *Appl. Opt.* 11 (1972) 613–616, <https://doi.org/10.1364/AO.11.000613>.
- [9] T.K. Chan, M. Megens, B.-W. Yoo, J. Wyras, C.J. Chang-Hasnain, M.C. Wu, D. A. Horsley, Optical beamsteering using an 8×8 MEMS phased array with closed-loop interferometric phase control, *Opt. Exp.* 21 (2013) 2807–2815, <https://doi.org/10.1364/OE.21.002807>.
- [10] Y. Wang, G. Zhou, X. Zhang, K. Kwon, P.-A. Blanche, N. Triesault, K. Yu, M.C. Wu, 2D broadband beamsteering with large-scale MEMS optical phased array, *Optica* 6 (2019) 557–562, <https://doi.org/10.1364/OPTICA.6.000557>.
- [11] J. Sun, E. Timurdogan, A. Yaacobi, E.S. Hosseini, M.R. Watts, Large-scale nanophotonic phased array, *Nature* 493 (2013) 195–199, <https://doi.org/10.1038/nature11727>.
- [12] T. Fukui, Y. Kohno, R. Tang, Y. Nakano, T. Tanemura, Single-pixel imaging using multimode fiber and silicon photonic phased array, *J. Lightwave Technol.* 39 (2021) 839–844, <https://doi.org/10.1109/JLT.2020.3008968>.
- [13] S. Chung, H. Abediasl, H. Hashemi, A monolithically integrated large-scale optical phased array in silicon-on-insulator CMOS, *IEEE J. Solid-State Circ.* 53 (2018) 275–296, <https://doi.org/10.1109/JSSC.2017.2757009>.
- [14] H. Abediasl, H. Hashemi, Monolithic optical phased-array transceiver in a standard SOI CMOS process, *Opt. Exp.* 23 (2015) 6509–6519, <https://doi.org/10.1364/OE.23.006509>.
- [15] F. Ashtiani, F. Aflatouni, $N \times N$ optical phased array with $2N$ phase shifters, *Opt. Exp.* 27 (2019) 27183–27190, <https://doi.org/10.1364/OE.27.027183>.
- [16] C. Zhao, C. Peng, W. Hu, Blueprint for large-scale silicon optical phased array using electro-optical micro-ring pixels, *Sci. Rep.* 7 (2017) 17727, <https://doi.org/10.1038/s41598-017-18040-3>.
- [17] H. Zhang, Z. Zhang, J. Lv, C. Peng, W. Hu, Fast beam steering enabled by a chip-scale optical phased array with 8×8 elements, *Opt. Commun.* 461 (2020) 125267, <https://doi.org/10.1016/j.optcom.2020.125267>.
- [18] J.K. Doyle, M.J.R. Heck, J.T. Bovington, J.D. Peters, L.A. Coldren, J.E. Bowers, Two-dimensional free-space beam steering with an optical phased array on silicon-on-insulator, *Opt. Exp.* 19 (2011) 21595–21604, <https://doi.org/10.1364/OE.19.021595>.
- [19] D. Kwong, A. Hosseini, J. Covey, Y. Zhang, X. Xu, H. Subbaraman, R.T. Chen, On-chip silicon optical phased array for two-dimensional beam steering, *Opt. Lett.* 39 (2014) 941–944, <https://doi.org/10.1364/OL.39.000941>.
- [20] M.J.R. Heck, Highly integrated optical phased arrays: photonic integrated circuits for optical beam shaping and beam steering, *Nanophotonics* 6 (2017) 93–107, <https://doi.org/10.1515/nanoph-2015-0152>.
- [21] M. Chul Shin, A. Mohanty, K. Watson, G.R. Bhatt, C.T. Phare, S.A. Miller, M. Zadka, B.S. Lee, X. Ji, I. Datta, M. Lipson, Chip-scale blue light phased array, *Opt. Lett.* 45 (7) (2020) 1934.
- [22] N.A. Tyler, D. Fowler, S. Malhouitre, S. Garcia, P. Grosse, W. Rabaud, B. Szelag, SiN integrated optical phased arrays for two-dimensional beam steering at a single

- near-infrared wavelength, *Opt. Exp.* 27 (2019) 5851–5858, <https://doi.org/10.1364/OE.27.005851>.
- [23] J. Midkiff, K.M. Yoo, J.-D. Shin, H. Dalir, M. Teimourpour, R.T. Chen, Optical phased array beam steering in the mid-infrared on an InP-based platform, *Optica*. 7 (2020) 1544–1547, <https://doi.org/10.1364/OPTICA.400441>.
- [24] K. Komatsu, Y. Kohno, Y. Nakano, T. Tanemura, Large-scale monolithic InP-based optical phased array, *IEEE Photon. Technol. Lett.* 33 (2021) 1123–1126, <https://doi.org/10.1109/LPT.2021.3107277>.
- [25] W. Xie, T. Komljenovic, J. Huang, M. Tran, M. Davenport, A. Torres, P. Pintus, J. Bowers, Heterogeneous silicon photonics sensing for autonomous cars [Invited], *Opt. Exp.* 27 (2019) 3642–3663, <https://doi.org/10.1364/OE.27.003642>.
- [26] N. Dostart, B. Zhang, A. Khilo, M. Brand, K. Al Qubaisi, D. Onural, D. Feldkhun, K. H. Wagner, M.A. Popović, Serpentine optical phased arrays for scalable integrated photonic lidar beam steering, *Optica*. 7 (6) (2020) 726.
- [27] M. Jacques, A. Samani, E. El-Fiky, D. Patel, Z. Xing, D.V. Plant, Optimization of thermo-optic phase-shifter design and mitigation of thermal crosstalk on the SOI platform, *Opt. Exp.* 27 (8) (2019) 10456.
- [28] S. Sabouri, L.A. Mendoza, M. Catuneanu, M. Namdari, K. Jamshidi, Thermo optical phase shifter with low thermal crosstalk for SOI strip waveguide, *IEEE Photon. J.* 13 (2) (2021) 1–12.
- [29] S. De, R. Das, R.K. Varshney, T. Schneider, CMOS-compatible photonic phase shifters with extremely low thermal crosstalk performance, *J. Lightwave Technol.* (2020) 1.
- [30] Junfeng Song, Q. Fang, S.H. Tao, T.Y. Liow, Fast and low power Michelson interferometer thermo-optical switch on SOI, *Optics Exp.*, 2008.
- [31] Q. Fang, J.F. Song, T.-Y. Liow, H. Cai, M.B. Yu, G.Q. Lo, D.-L. Kwong, Ultralow power silicon photonics thermo-optic switch with suspended phase arms, *IEEE Photon. Technol. Lett.* 23 (2011) 525–527, <https://doi.org/10.1109/LPT.2011.2114336>.
- [32] M.R. Watts, J. Sun, C. DeRose, D.C. Trotter, R.W. Young, G.N. Nielson, Adiabatic thermo-optic Mach-Zehnder switch, *Opt. Lett.* 38 (2013) 733–735, <https://doi.org/10.1364/OL.38.000733>.
- [33] G. Kang, C.-H. Youn, K. Yu, H.-H. Park, S.-H. Kim, J.-B. You, D.-S. Lee, H. Yoon, Y.-G. Ha, J.-H. Kim, D.-E. Yoo, D.-W. Lee, Silicon-based optical phased array using electro-optic p-i-n phase shifters, *IEEE Photonics Technol. Lett.* 31 (21) (2019) 1685–1688.
- [34] D. Yi, W. Zhou, Y. Zhang, H.K. Tsang, Inverse design of multi-band and wideband waveguide crossings, *Opt. Lett.* 46 (4) (2021) 884.
- [35] H.L. Han, H. Li, X.P. Zhang, A. Liu, Y.F. Chen, High performance ultra-compact SOI waveguide crossing, *Opt. Exp.* 26 (2018) 25602.
- [36] D. Melati, M. Kamandar Dezfouli, Y. Grinberg, J.H. Schmid, R. Cheriton, S. Janz, P. Cheben, D.-X. Xu, Design of compact and efficient silicon photonic micro antennas with perfectly vertical emission, *IEEE J. Select. Top. Quant. Electron.* 27 (1) (2021) 1–10.
- [37] Y.Y. Zhang, R. Wang, R.T. Jiang, K.Y. Du, Y.Y. Li, Optimal design of silicon based optical phased array sector antenna, *Infra. Laser Eng.* 50 (2021) 8.
- [38] K.Y. Du, R. Wang, J. Guo, R.T. Jiang, D.B. Kan, Y.Y. Zhang, Design of a sparse array for a one-dimensional non-uniform optical phased array, *J. Opt. Soc. Am. B* 39 (2022) 1141–1146.